Green solid-state synthesis of Cu_4O_3/biochar composites with high antimicrobial activity

Ke Sun
Shanghai University
Wenyi Yang
Shanghai University
Yiheng Shen
Shanghai University
Zihan Wang
Shanghai University
Yindian Wang
Shanghai University
Hongxia Chen
hxchen@shu.edu.cn

Shanghai University
Yi Liu
yiliu@shu.edu.cn

Shanghai University

Research Article

Keywords: Cu4O3/biochar composite, solid-state synthesis, symproportionation reaction, antimicrobial material, superbug

Posted Date: August 9th, 2024

DOI: https://doi.org/10.21203/rs.3.rs-4879778/v1

Additional Declarations: The authors declare no competing interests.

Abstract

Infectious diseases caused by pathogenic microorganisms have inflicted significant calamities upon human society. The Cu_4O_3/biochar composites with high efficacy of antimicrobial properties are developed for the first time via a green solid synthesis strategy of ball milling and sintering processes in this work. The mechanistic investigation revealed that the biochar, e.g. corn stover, plays multiple physiochemical roles as a support carrier, dispersant, and reducing agent, regulating elegantly the stoichiometric ratio of Cu_2O and CuO. The potent antimicrobial activities of the Cu_4O_3/biochar composite were confirmed against E. coli, S. aureus, and methicillin-resistant Staphylococcus aureus MRSA through minimum inhibitory concentration (MIC) testing, exhibiting extremely low MIC values against the Gram-positive strains S. aureus and MRSA. Furthermore, the antibacterial mechanisms of the Cu_4O_3/biochar composite were studied through the experiments and quantum mechanical computations, showing the enhanced effects between the successive release of Cu(I)/Cu(II) ions and the generation of reactive oxygen species. This work reports the first solid-state symproportionation reactions of CuO_x to prepare high-purity Cu_4O_3, stabilized by biochar with the advantages of simplicity, low cost, brevity, mild reaction conditions, and eco-friendliness. The Cu_4O_3/biochar composite can be applied as additives in anti-bacterial materials to protect against harmful microbial infections including superbugs.

1. Introduction

Infectious diseases caused by pathogenic microorganisms have brought severe mortality, social issues, and economic losses to human society.[1] Antimicrobial resistance (AMR) induced by the use or misuse of antibiotics, has emerged as one of the foremost global threats to public health and development.[2] In 2019, AMR caused directly 1.27 million deaths worldwide, with an additional 4.95 million deaths attributed indirectly.[3] Failure to take sufficient action to control AMR is forecasted to escalate annual mortality to approximately 10 million by 2050.[2b]

Copper oxides (Cu_xO), such as Cu_2O and CuO have demonstrated significant potential in antimicrobial applications against pathogenic microorganisms due to their high efficiency antimicrobial, antifungal, and antiviral properties as well as their low costs and environment benign.[4] Cu_4O_3, also known as paramelaconite, was initially discovered in the 1870s at the Copper Queen Mine in Bisbee, Arizona, USA, and represents one of the least studied Cu_xO.[5] Its unique structure exhibits the characteristics with a mixed copper valence states and lattice positioned between Cu_2O and CuO, constituting a metastable intermediate compound containing both Cu(I) and Cu(II) ions.[6]

After more than 100 years since its initial discovery, the explicit synthetic pathway for Cu_4O_3 was first reported in 1996: Morgan et al. prepared Cu_4O_3 by extracting copper or its oxides with concentrated ammonia in a Soxhlet apparatus. However, the quantitative analysis revealed that the synthesized

product consisted of 35% Cu_4O_3, 27% Cu_2O, and 38% CuO. The low purity of Cu_4O_3 may be attributed to the challenge of stabilizing both Cu(I) and Cu(II) ions in the solution system.[5] Additionally, Cu_4O_3 is thermodynamically unstable and can decompose easily into Cu_2O and CuO during the preparation process.[6–7] Subsequent studies have explored gas-phase synthesis methods, such as chemical vapor deposition (CVD) or sputtering deposition, for preparing pure phases of Cu_4O_3 or partially containing Cu_4O_3.[8] For instance, Blobaum et al. reported the preparation of Cu_4O_3 thin films by sputter deposition on CuO targets. However, the yield was only at the milligram level, and the morphology and purity of the products were significantly affected by factors such as oxygen partial pressure and substrate temperature.[8a] The other studies prepared Cu_4O_3 or its composites by liquid phase chemistry methods such as solvothermal or wet chemistry methods.[9] Zhao et al. synthesized phase-pure Cu_4O_3 microspheres by the solvothermal method under solvent conditions of N, N-dimethylformamide (DMF), and ethanol with $Cu(NO_3)_2$ as the precursor.[9b] However, Jiang et al. attempted to replicate Zhao's work but with less satisfactory results, yielding only impure phase Cu_4O_3 in the product.[7] Liquid-phase chemistry for the preparation of Cu_4O_3 still faces challenges such as process complexity, lack of control, low yield, and difficulty in obtaining the high-purity Cu_4O_3. The low-cost, large-scale synthesis of high-purity Cu_4O_3 and the maintenance of their stability still pose a great challenge, hindering the further exploration of their properties and applications.

Biochar is one of the carbonaceous materials prepared through the pyrolytic carbonization of biomass, (e.g., crop and forestry residues, manure, and solid organic wastes from urban and industrial sources) in an O_2-limited/free environment.[10] The high specific surface area, rich porous structure, oxygenated functional groups on the surface, and flaky aromatic structure confer rich physicochemical properties and application potential to biochar.[10a] In recent years, biochar has found widespread use in soil improvement, sewage treatment, air purification, carbon sequestration, and emission reduction.[11] Supporting various functional metal oxide particles onto biochar to synthesize biochar-based composites can combine the respective advantages of both parties, enhance the dispersion and stability, improve the application performance of the functional particles, and endow biochar with new application capabilities.[12] In addition to the physical support and stabilization, biochar substrate exhibits a unique redox capacity from the chemistry point of view.[13] The recent studies have focused on preparing biochar-based composites through the supporting capacity and redox property of biochar, applied to various applications such as pollutant adsorption, water treatment, and antibacterial agents.[12a, 14]

In this study, we present for the first time *in-situ* preparation of Cu_4O_3/biochar (e.g., corn stover) composite via a solid-state synthesis strategy combining ball milling and sintering processes in air. In this preparation process, copper formate serves as the copper source, while biochar acts as the support carrier, dispersant, and reducing agent. Compared with the preparation methods of Cu_4O_3 reported previously, the solid-state preparation approach displays advantages such as facile, a concise short process flow, controllability, and mild conditions, without the need for any oxidizing or reducing chemical

reagents, and little generation of solid/liquid waste, coinciding with the concept of “green chemistry” manufacture. We systematically investigated the crystal structure, purity, valence state, morphology, and loading amount of Cu_4O_3/biochar composite through various characterization methods, with the elucidation of the preparation process and mechanism. Through minimum inhibitory concentration (MIC) antibacterial testing and bacterial morphology analysis, we demonstrated the highly efficient antibacterial properties of the Cu_4O_3/biochar composite against Escherichia coli *E. coli*, Staphylococcus aureus *S. aureus*, and Methicillin-resistant Staphylococcus aureus *MRSA*. Notably, the Cu_4O_3/biochar composite displayed remarkably low MIC values (0.100 μg/mL and 0.125 μg/mL, respectively) against Gram-positive strains *S. aureus* and *MRSA*. Furthermore, we systematically investigated the antibacterial mechanism and the stability in solution of the Cu_4O_3/biochar composite through experimental methods coupled with calculations, demonstrating for the first time the Cu-ion precipitation mechanism of Cu_4O_3 formation. The Cu_4O_3/biochar composite is anticipated to be applied in public facilities and healthcare environments, imparting surfaces with heightened resistance to infection by pathogenic microorganisms, including superbugs. The synthesis approach developed in this work realized the first solid-state CuO_x symproportionation reactions and prepared the Cu_4O_3/biochar composites by combining ball milling and sintering processes. The solid-state symproportionation (SSS) approach can be extended to achieve large-scale preparation and facilitate more fundamental studies and potential applications of Cu_4O_3.

2. Results and Discussion

2.1 Preparation and characterization of the Cu_4O_3/biochar composite

Figure 1. depicts schematically the solid-state preparation process for the Cu_4O_3/biochar composite through two-stage ball millings followed by sintering processes. The corn stover biochar (CSBC) was first derived from corn stover via grinding and washing, followed by slow pyrolysis.[15] Copper formate underwent the successive ball milling process (BM-1) and subsequent co-ball milling with the CSBC (BM-2) to obtain the copper formate/CSBC precursor. The SEM images (Figure S1, Supporting Information) illustrate that the BM-1 process refined the particle size of copper formate from the initial micron-sized flakes to uniformly distributed submicron particles.[16] The CSBC underwent a co-ball milling process (BM-2) with copper formate resulting in the transformation of its initial irregular morphology and unevenly sized particles into small particles with uniform sizes (5–20 μm) (Figure S2a-b, Supporting Information), demonstrating the effectiveness of the ball milling process in reducing the biochar sizes.[17] Moreover, the submicron copper formate particles served as grinding balls to assist in grinding the biochar.[18] Furthermore, copper formate particles exhibited uniform and dense distribution on the surface of CSBC (Figure S2c-d, Supporting Information). Ultimately, the Cu_4O_3/CSBC composite was

obtained via the solid-state sintering process at 230 ℃ for 12 minutes. The parameters of sintering processing were carefully optimized as discussed later.

The crystal structure of the Cu_4O_3/CSBC composite was initially analyzed using X-ray diffraction (XRD). As illustrated in Fig. 2a, CSBC exhibited typical broad and gradual amorphous carbon diffraction peaks at 2θ = 15–30°;[19] the X-ray diffraction peaks appearing at 28.2°, 30.7°, 35.7°, 36.3°, 44.0°, 58.3°, 63.9°, 65.0°, and 75.5° can be assigned to the (112), (200), (202), (004), (220), (224), (400), (206), and (422) crystal planes of Cu_4O_3. All these diffraction peaks were consistent with the characteristic peaks of the Cu_4O_3 standard card (JCPDS No.49-1830), and no diffraction peaks from other copper compounds were observed, such as Cu, CuO, and Cu_2O, indicating that the Cu_4O_3/CSBC composite contains high purity Cu_4O_3.

X-ray photoelectron spectroscopy (XPS) was employed to further evaluate the valence states of the Cu_4O_3/CSBC composite. The presence of elemental Cu signal peaks confirmed the deposition of elemental Cu on the biochar surface, as illustrated in the XPS spectra (Fig. 2b). The Cu $2p_{3/2}$ XPS spectrum (Fig. 2c) displays the fitted peaks at 932.8 eV and 934.8 eV attributed to Cu(I) and Cu(II) ions, respectively.[9a] The XPS spectra confirm that Cu_4O_3 is a mixed-valence compound comprising both Cu(I) and Cu(II) ions. Moreover, the content of Cu element in the Cu_4O_3/CSBC composite was detected by the inductively coupled plasma-optical emission spectrometry (ICP-OES), the mass ratio of Cu is 12.87 wt.%, indicating the content of Cu_4O_3 is 15.30 wt.% (Table S1, Supporting Information) according to the mass ratio (84.1%) of Cu element relative to Cu_4O_3. This value coincides with our predetermined experimental value, indicating that the solid-synthesis strategy can achieve the quantitatively controllable preparation of the contents of Cu_4O_3 in the Cu_4O_3/CSBC composite.

The structural composition of the Cu_4O_3/CSBC composite was examined using Fourier-transform infrared (FTIR) spectroscopy (Fig. 2d). The Cu_4O_3/CSBC composite exhibited absorption bands resembling those of the CSBC at wavelengths of 3425 cm^{-1}, 2920 cm^{-1}, 1720 cm^{-1}, and 1610 cm^{-1}, representing -OH, C-H, -C = O, and -C = C stretching vibrations, respectively.[20] However, the absorption bands related to -C = O and -C = C of aromatic groups appeared more pronounced, while the $-CH_2$ band intensity decreased compared to the characteristic absorption bands of CSBC. The escalation in oxygen-containing functional groups and the decline in methyl groups of the biochar could be attributed to intense mechanical collision during the BM-2 process and the thermal oxidation process by O_2 during the solid-state sintering process.[17a, 21] Additionally, three signal bands corresponding to the Cu-O stretching vibration of Cu_4O_3 were detected at wavelengths of 616 cm^{-1}, 547 cm^{-1}, and 470 cm^{-1},[9a] further indicating the high purity of Cu_4O_3 within the Cu_4O_3/CSBC composite.

The microscopic morphology and elemental distribution of the Cu_4O_3/CSBC composite were investigated using scanning electron microscopy (SEM), transmission electron microscopy (TEM), and energy-dispersive X-ray spectroscopy (EDX) elemental mapping. The macroscopic SEM image (Fig. 2e)

illustrates the uniform particle size distribution of the Cu_4O_3/CSBC composite. The microscopic SEM images (Fig. 2f-g) at various magnifications reveal the uniform and dispersed distributions of Cu_4O_3 nanoparticles that form clusters on the surface of the CSBC. The morphology of Cu_4O_3 was further elucidated by TEM analysis, confirming the cluster structures formed by many fine nanoparticles (Fig. 2h-i). The high-resolution transmission electron microscopy (HRTEM) image (Fig. 2j) displays the distinct lattice streaks with a lattice spacing of 0.25 nm corresponding to the (202) crystal plane of Cu_4O_3 crystal (JCPDS No.49-1830). The EDX elemental mapping (Fig. 2k) indicates a homogeneous spatial arrangement of Cu and O elements within the Cu_4O_3 nano-sized clusters, consistent with the TEM images.

We further investigated the influence of the preparation processing parameters, e.g. sintering temperature/time and loading capacity, on the reaction products. When the solid-state sintering was conducted at 220 ℃ for 12 min, copper formate was not completely decomposed and impurities of Cu_2O and CuO appeared in the sintered products (Figure S3a, Supporting Information). At a sintering temperature of 240 ℃, the XRD analysis reveals the presence of Cu_2O and CuO impurities in the products (Figure S3b, Supporting Information), indicating the decomposition of partial Cu_4O_3 to Cu_2O and CuO at 240 ℃, consistent with the reported transition temperature of Cu_4O_3.[9b] Subsequently, we assessed the supporting capacity of CSBC for Cu_4O_3. When the supporting ratio of Cu_4O_3 was 10 wt.%, the solid-state sintered products exhibited pure-phase Cu_4O_3 (Figure S4a, Supporting Information); however, attempting to support 20 wt.% of Cu_4O_3 resulted in sintered products containing Cu_2O and CuO impurities (Figure S4b, Supporting Information). The appearance of impurity by-products in the sintering process may be caused by the heat released from the decomposition of copper formate that could cause the decomposition of Cu_4O_3[22].

In order to assess the generalizability of various biochar sources for the preparation of Cu_4O_3/biochar composite, we explored the impact of biochar derived from different biomass sources (e.g., palm leaves, cedar wood, and bagasse) on the sintered products. Figure 3(a-c) displays the XRD spectra of the sintered products resulting from various biochar (named PLBC, CWBC, and BBC, respectively) prepared from palm leaves, cedar wood, and bagasse as biochar feedstock sources after the ball milling (BM-2) and sintering processes with copper formate. Among these, copper formate/PLBC precursor yielded the Cu_4O_3/PLBC composite containing pure-phase Cu_4O_3 (Fig. 3a); copper formate/CWBC precursor accommodated a support amount of 10 wt.% Cu_4O_3 without impurities (Fig. $3b_I$) while attempts to support 15 wt.% Cu_4O_3 led to impurities of Cu_2O and CuO in the sintered products (Fig. $3b_{II}$), which may be due to the differences in specific surface area and supporting capacity among the various biochar types.[12a] At a pyrolysis temperature of 300 ℃ for bagasse biochar, the sintered product contained the impurity of Cu_2O, in addition to Cu_4O_3 (Fig. $3c_I$). However, at a pyrolysis temperature of 400 ℃, the sintered product obtained showed high purity Cu_4O_3 (Fig. $3c_{II}$). The optimal processing parameters for preparing Cu_4O_3/biochar composite from PLBC, CWBC, and BBC are listed in Table S2.

Subsequently, the morphology of the Cu_4O_3/biochar composite obtained from different sources of biochar was analyzed by SEM. As depicted in Fig. $3a_1$, $3b_1$, and $3c_1$, the biochar inherited the morphology and characteristics of the corresponding biomass before undergoing the Cu_4O_3/biochar composite preparation process. In contrast, the morphology and structure of the sintered products were relatively similar in that Cu_4O_3 nanoparticle clusters were uniformly dispersed on the surface of the biochar particles with consistent particle sizes (Fig. $3a_{2\text{-}3}$, $3b_{2\text{-}3}$, and $3c_{2\text{-}3}$). The exploration of biochar feedstock sources experiments demonstrated that the preparation process of Cu_4O_3/biochar composite through ball milling combined with sintering processes exhibits a certain degree of generalizability. Nevertheless, the functional groups, specific surface area, and supporting capacity of biochar derived from various feedstock sources,[23] necessitating adjustments to the pyrolysis parameters or the preparation process based on the specific raw feedstock when preparing the Cu_4O_3/biochar composite. In general, all the studied Cu_4O_3/biochar composites can be prepared successfully while their optimal processing parameters may vary depending on the biochar resources.

2.2 Formation mechanism of the Cu_4O_3/CSBC composite

To investigate the formation mechanism of the Cu_4O_3/CSBC composite, we employed a rapid cooling method using liquid nitrogen to quench the chemical reactions during the process of solid-state sintering to identify intermediate phases in the evolution of sintering reactions.[16] Fig. 4a illustrates the comparative XRD spectra of the sintered products derived from copper formate/CSBC precursor during various sintering times (0–12 min) at 230 ℃. As the sintering time prolonged, the intensity of the signal XRD peaks corresponding to copper formate diminished gradually and disappeared completely at 10 min, indicating its rapid decomposition process. Furthermore, three distinct signal peaks of Cu_4O_3, Cu_2O, and CuO emerged simultaneously during the intermediate stages. The diffraction peak intensities of Cu_2O and CuO initially increased, then weakened, and disappeared eventually at 12 min, indicating the formation and subsequent disappearance of intermediate phases involving Cu_2O and CuO. These observations discovered the formation of intermediate phases Cu_2O and CuO during the sintering process, suggesting that Cu_4O_3 should originate from Cu_2O and CuO via the solid-state symproportionation reactions between Cu_2O and CuO.[9b] Such symproportionation reaction among Cu_xO was originally proposed in liquid phase reactions[9b], but it is for the first time demonstrated in solid-state reactions in this work to our best knowledge.

In our previous study,[16] we analyzed the thermal decomposition process of copper formate. Copper formate undergoes two consecutive stepwise cation reduction processes to generate Cu, which is subsequently oxidized by O_2 to form Cu□O and CuO. However, in the absence of any carrier or medium, Cu_2O and CuO cannot directly disproportion into Cu_4O_3 in air. We further investigated the critical role of CSBC in the preparation process of Cu_4O_3/CSBC composite through a series of controlled experiments. The specifically designed processing processes are shown in Table S3 (Supporting Information), including untreated CSBC (CSBC), CSBC treated with the BM-2 process (BM-CSBC), CSBC treated with

BM-2 followed by sintering processes (BM-S-CSBC), and the Cu_4O_3/CSBC composite. Figure 4b illustrates the C 1s spectra and their fitting results of CSBC after different preparation processes. Copper formate participates in the BM-2 process with CSBC, so we excluded the influence of formate groups in copper formate on the fitting results of C1s through filtration and washing after BM-2 in the controlled experiments for the samples BM-CSBC and BC-S-CSBC. As can be seen in Fig. 4b, the comparisons of C 1s among the CSBC, BM-CSBC, and BM-S-CSBC samples exhibited an increase in the contents of oxygen-containing functional groups C = O and O-C = O. The normalized quantitative analysis of C 1s spectra fitting results (Fig. 4c) further clarifies this phenomenon. Furthermore, the content of C-C/C = C/C-H functional groups of BM-CSBC, and BM-S-CSBC samples decreased compared to that of CSBC. The analysis result indicates that the strong mechanical collisions during the BM-2 process and the thermal oxidation reaction in air during the sintering process increase the oxygen-containing functional groups of biochar and decrease the abundance of C-H functional groups,[17a, 21] which is consistent with the results of FTIR analysis. As a comparison, the relative contents of C = O and O-C = O in the Cu_4O_3/CSBC composite were notably higher compared with those in CSBC, BM-CSBC, and BM-S-CSBC, with a further reduction in C-H content, indicating the chemical role of biochar in additional oxidative processes, specifically participating in the redox conversion from CuO to Cu_2O.

Based on the analysis results above, we summarize schematically in Fig. 4d the preparation mechanism of the Cu_4O_3/CSBC composite. The two-step ball milling processes, BM-1 and BM-2, facilitate the uniform dispersion of refined copper formate particles onto the surface of CSBC. During the solid-state sintering process, copper formate underwent gradual cation reduction processes to generate Cu, which was then oxidized to Cu_2O by O_2 and further oxidized to CuO in air (Step 1 in Fig. 4d). The stoichiometric ratio of Cu_2O to CuO is crucial for the formation of high-purity Cu_4O_3[9b]. CSBC plays a crucial role in regulating the ratio of Cu_2O and CuO in the reaction system: its weak reduction capacity could reduce CuO partially into Cu_2O but not all. Subsequently, the CuO and Cu_2O mixtures with an appropriate 2:1 ratio underwent the symproportionation reaction to form Cu_4O_3 (Step 2 in Fig. 4d). Meanwhile, the strong mechanical collisions of BM-2, air thermal decomposition, and oxidation-reduction reaction with CuO, increased the content of oxygen-containing functional groups, e.g., C = O and O-C = O, and reduced that of the C-H groups of CSBC.

2.3 Antibacterial property

The antibacterial properties of the Cu_4O_3/CSBC composite were investigated using Gram-negative bacterium Escherichia coli *E. coli*, Gram-positive bacterium Staphylococcus aureus *S. aureus*, and methicillin-resistant Staphylococcus aureus *MRSA* as bacterial models. *MRSA* is a significant cause of hospital and community-associated infections, characterized by its multidrug resistance.[24] We evaluated the antibacterial efficacy of the Cu_4O_3/CSBC composite across various concentration gradients on three bacteria and determined the minimum inhibitory concentration (MIC) for each bacterium. Untreated CSBC and blank groups were applied as controls to evaluate the antibacterial activity of the Cu_4O_3/CSBC composite. As depicted in Fig. 5a, the antibacterial rate gradually declined

from > 99.9% as the concentration of Cu_4O_3/CSBC composite decreased, indicating a positive correlation between the bactericidal effect and concentration. At the concentration of 5 μg mL^{-1} for the Cu_4O_3/CSBC composite, *E. coli* was effectively eradicated and unable to proliferate on the nutrient medium. Notably, compared to the antibacterial effect against *E. coli*, the Cu_4O_3/CSBC composite showed lower MIC values against the Gram-positive bacteria *S. aureus* and *MRSA*: there were few surviving *S. aureus* or *MRSA* bacteria detected on the Petri dishes at concentrations of 0.100 μg mL^{-1} and 0.125 μg mL^{-1} of the Cu_4O_3/CSBC composite, respectively. The variation in the antibacterial efficacy of the Cu_4O_3/CSBC composite against Gram-negative and Gram-positive bacteria aligns with previously reported results regarding Cu_4O_3, potentially attributed to disparities in the cell membrane structure between the two bacterial strains.[25] In contrast, both the CSBC and blank (Fig. 5a). These results indicate that the MIC values of the Cu_4O_3/CSBC composite against *E. coli*, *S. aureus*, and *MRSA* were 5 μg mL^{-1}, 0.100 μg mL^{-1}, and 0.125 μg mL^{-1}, respectively (Table S4, Supporting Information). Compared with the previous reports on the antibacterial properties of Cu_4O_3,[9a] the antibacterial effect was enhanced by at least three orders of magnitude for the Cu_4O_3/CSBC composite in this work. Furthermore, we compared the MIC values of reported inorganic antibacterial materials against *MRSA* (Table 1). The Cu_4O_3/CSBC composite exhibits a significantly lower MIC value, indicating its efficient and notable antibacterial ability against superbug *MRSA*.

Furthermore, we applied SEM to observe the surface morphology of bacteria before and after treatment with the Cu_4O_3/CSBC composite (Fig. 5b). *E. coli* exhibited a rod-shaped morphology, while *S. aureus* and *MRSA* appeared spherical. Prior to the treatment, the bacteria displayed smooth surfaces with intact cell walls and membrane structures, but presented irregular morphologies with the wrinkling of the cell walls due to shrinkage after treated with the Cu_4O_3/CSBC composite.

Table 1
The MIC values comparison of inorganic antibacterial materials against *MRSA*.

Samples	MIC values for *MRSA* ($\mu g\ mL^{-1}$)	Refs.
Cu_4O_3/CSBC composite	0.125	this work
Ag NPs (average size: 8.55–20.3 nm)	8.125	[26]
Si-Ag	2500–5000	[27]
Graphene oxide-Ag nanocomposite (average size: 9.4 ± 2.8 nm)	15	[28]
Cu NPs (particle size: 50 nm)	1.875–3.75	[29]
CuO NPs (particle size: 40 nm)	75–150	[30]
Cu_2O@ZrP hybrid nanosheet	200	[4c]
ZnO nanorods	23 ± 1.09	[31]
ZnO NPs (average size: 20–25 nm)	125	[32]
Heterogeneous TiO_2/ZnO Nanocomposite	80–2500	[33]

2.4 Antibacterial mechanism

A number of studies have investigated the antibacterial mechanisms of CuO and Cu_2O, primarily focusing on the release of Cu ions, the induction and generation of reactive oxygen species (ROS), and direct contact with bacteria but few studies were carried out on Cu_4O_3.[34] In order to investigate the antibacterial mechanism of the Cu_4O_3/CSBC composite, we first analyzed the release kinetics of Cu ions from the Cu_4O_3/CSBC composite by ICP-OES test. As shown in Fig. 6a, the cumulative release of Cu ions exhibited a positive correlation with immersion time during the 48-hour testing period. The cumulative release of Cu ions reached 2.71 ppm within 48 h, with the highest release rate of 235 ppb h^{-1} occurring in the initial 2 h (Figure S5, Supporting Information). The rapid release ensures the highly efficient antibacterial performance of the Cu_4O_3/CSBC composite. With prolonged immersion time, the Cu ions release rate decelerated gradually, which may be caused by the adsorption of copper ions by CSBC,[35] indicating a slow-release process that ensures long-lasting antibacterial efficacy.

Both Cu(I) and Cu(II) ions have been reported to possess antibacterial effects and can induce the production of ROS by the redox reaction. Notably, the antibacterial efficacy of Cu(I) ions is significantly

stronger than that of Cu(II) ions.[36] Despite exhibiting a mixed valence of Cu(I) and Cu(II) at the Cu 2p XPS spectrum, the release mechanism of copper ions in Cu_4O_3 remains poorly understood. Initially, we detected the release of Cu(I) ions using bathocuproinedisulfonic acid disodium salt (BCS) as a specific chelator of Cu(I) ions. BCS can form stable complexes with Cu(I) ions, characterized by typical absorption peaks in the range of 450–500 nm.[37] To minimize testing errors resulting from the oxidation of Cu(I) ions,[38] we conducted an anaerobic condition for the solution system. As depicted in Fig. 6b, the control BCS exhibited no absorbance within the wavelength of 450–500 nm, while the absorbance of BCS treated with the Cu_4O_3/CSBC composite displays a characteristic absorption peak at 483 nm.[37] The absorbance exhibited a gradual increment over the 48-hour test period, indicating a slow-release kinetics of Cu(I) ions within the Cu_4O_3/CSBC composite. Furthermore, we obtained the linear regression equation by measuring the standard curve between the absorbance of BCS at 483 nm and the concentration of Cu(I) ions (Figure S6, Supporting Information), thereby quantitatively evaluating the release of Cu(I) ions (Figure S7, Supporting Information). Then, the release concentration of Cu(II) ions was obtained by the difference between the total release concentration of Cu ions (ICP-OES results) and the release concentrations of Cu(I) ions. As can be seen in Figure S7 (Supporting Information), the cumulative release of Cu(II) ions also increased continuously during the 48-hour immersion experiment.

To further investigate the solvation mechanism of copper ions in Cu_4O_3, density functional theory (DFT) calculations were performed to compute the vacancy formation energy of Cu. Figure 6c illustrates the ball-and-stick model of Cu_4O_3 with body-centered tetragonal lattice structure (No.141, $I4_1/amd$ space group), characterized by the built of inter-penetrating chains of Cu(I)-O and Cu(II)-O.[39] The (101) surface model of Cu_4O_3 was constructed and optimized (Fig. 6d), containing three types of copper: monovalent copper (Cu-I), tetra-coordinated divalent copper (Cu-II-a), and tri-coordinated divalent copper (Cu-II-b). Subsequently, the vacancy formation energies of these copper types (Fig. 6e) were calculated using density functional theory (DFT). The calculation results (Table S5, Supporting Information) indicate that Cu-I exhibits the lowest vacancy formation energy, suggesting that Cu(I) ions are more easily dissolved than Cu-II-a and Cu-II-b ions. Additionally, the (100) surface model was constructed to calculate the vacancy formation energies of Cu-I and Cu-II (Fig. 6f). The results (Table S6, Supporting Information) demonstrate that the vacancy formation energy of Cu-I is lower than that of Cu-II again, consistent with the results of the (101) surface. These DFT calculations suggest that Cu(I) ions may dissolve more easily than Cu(II) ions from the surface of Cu_4O_3, and thus participate more efficiently in the antimicrobial process. The varied vacancy formation energies on the surfaces suggest the successive dissolution of Cu(I) followed by Cu(II) ions that may contribute to the long-lasting antimicrobial performance via the Cu-ion release mechanism.

Moreover, the stability of Cu_4O_3/CSBC composite in solution is critical. We confirmed the good chemical stability of the Cu_4O_3/CSBC composite by the 48-hour immersion in aqueous solution through comparison of XRD spectra (Fig. 6g). No obvious peaks were detected corresponding to Cu_2O, CuO, or Cu. Additionally, the intensity of Cu_4O_3 diffraction peaks gradually decreased with prolonged immersion

time. We selected the strongest intensity of the XRD diffraction peak, (202), as the representative peak and compared it with the intensity of the amorphous diffraction peak of CSBC ($I_{d(202)}/I_{d(CSBC)}$). The comparison results (Table S7, Supporting Information) revealed that the ratio of $I_{d(202)}/I_{d(CSBC)}$ decreased with increasing immersion time, further demonstrating the gradual release process of Cu ions from Cu_4O_3.

Subsequently, we assessed the generation of superoxide anion ($\bullet O_2^-$) using nitroblue tetrazolium (NBT) as reactant to evaluate the ROS generation capacity of the Cu_4O_3/CSBC composite.[40] $\bullet O_2^-$ can reduce NBT to water-insoluble formazan.[41] Fig. 6h illustrates the absorbance changes of the NBT solution over 60 min after the addition of Cu_4O_3/CSBC composite. Compared to the NBT solution control, the intensity of the absorption peak at 259 nm significantly decreased after 10 min of adding the Cu_4O_3/CSBC composite, indicating the generation of $\bullet O_2^-$.[41] Over time, the absorbance of the NBT solution declined steadily, signifying the continuous degradation of NBT and a gradual rise in the concentration of $\bullet O_2^-$. These above results indicate that the Cu_4O_3/CSBC composite can produce ROS and participate in the antibacterial mechanism.

Based on the above analysis, we summarize the antibacterial mechanism of the Cu_4O_3/CSBC composite as illustrated in Fig. 6i. The antibacterial efficacy of inorganic antibacterial agents is heavily influenced by their particle size, morphology, and dispersion.[16] The Cu_4O_3/CSBC composite contains well-dispersed nano-sized Cu_4O_3, forming the foundation for their potent antibacterial activity and strong affinity for bacterial cells. Bacteria possess negatively charged cell surfaces, and the sustained slow release of Cu(I) and Cu(II) ions from the Cu_4O_3/CSBC composite can adhere to the bacterial surfaces, enhancing cell permeability and disrupting the cell walls/membrane structures to facilitate penetration of Cu ions into the cell interior. Concurrently, Cu(I) and Cu(II) ions, in conjunction with dissolved oxygen in water, participate in the production of ROS.[36c] The disruption of the cell membrane facilitates the entry of more Cu ions and ROS into the cell interior. Within the cell, Cu ions further stimulate ROS generation, leading to DNA denaturation, lipid and protein structural damage, culminating in cell death.

3. Materials and methods

3.1. Materials

Basic copper carbonate ($CuCO_3{\cdot}Cu(OH)_2$, 54–56% Cu, pure), formic acid (99% pure), anhydrous zinc acetate (99.5% pure), and anhydrous ethanol (99.8% pure) were purchased from Shanghai Macklin Biochemical Co., Ltd. All reagents were used without further purification.

Corn straw, palm leaves, bagasse, and fir branches are used as raw materials for the preparation of biochar. Among them, corn straw was collected from farmland in Zibo, Shandong province, China; Palm leaves and fir branches were collected from the campus of Shanghai University, China; Bagasse comes from sugarcane purchased from a fruit store.

3.2. Bacteria

Bacterial strains *Gram-negative Escherichia coli* (ATCC 25922), *Gram-positive Staphylococcus aureus* (ATCC 6538), and Methicillin-resistant Staphylococcus aureus *MRSA* (ATCC 43300) were purchased from the American Type Culture Collection (ATCC, USA).

3.3. Materials characterizations

X-ray diffraction (XRD) spectrum was measured by the Bruker-D2 PHASE X-ray diffraction system (Cu Kα radiation, λ = 1.54184 Å, Bruker, Germany). The morphology and chemical compositions were analyzed by scanning electron microscopy (SEM, Sigma 500, Zeiss, Germany), transmission electron microscopy (TEM, accelerating voltage: 300 kV, FEI THEMIS ETEM G3, Thermo Fisher, US), and energy-dispersive X-ray spectrum (EDX) elemental mapping (80T, Oxford, UK), respectively. The surface chemical states of samples were measured by X-ray photoelectron spectroscopy (XPS, Al Kα source, Escalab Xi+, Thermo Fisher, US), and the whole data was corrected by C 1s value (284.8 eV). The structural composition of the Cu_4O_3/CSBC composite was examined using Fourier-transform infrared spectroscopy (FTIR, Nicolet iS50, Thermo Fisher Scientific, US). The content of Cu was measured by inductively coupled plasma-optical emission spectrometry (ICP-OES, 730 Series, Agilent Technologies, US). The Cu content of the sample was calculated from the element analysis obtained via ICP-OES. The morphology of bacteria was observed by SEM (NOVA NanoSEM 450, FEI, US). The absorbance of the samples was analyzed by Ultraviolet-visible (UV-vis) spectra (UV-2450, Shimadzu, Japan).

3.4. Methods

3.4.1. Preparation of the Cu_4O_3/biochar composite

Preparation of biochar and copper formate

Corn stover biochar (CSBC) was prepared by slow pyrolysis method in an Ar atmosphere.[10b] Corn stover underwent cutting and pulverization, followed by sequential washing three times with deionized water and anhydrous ethanol separately to eliminate potential ionic impurities. Subsequently, the powder was dried at 70 ℃ for 2 h. The dried corn stover powder was placed into a quartz crucible and then transferred into a tube furnace. After post-Ar displacement, the furnace was heated to 300 ℃ at a heating rate of 10 ℃ min^{-1} under Ar atmosphere and maintained for 2 hours. Upon cooling to room temperature, the sample was retrieved from the furnace to obtain CSBC.

Copper formate was prepared by precipitation reaction using basic copper carbonate and 30% formic acid aqueous solution.[16]

Ball milling process (BM-1 and BM-2)

BM-1: The BM-1 process for copper formate has followed the method outlined in our previous work.[16] In brief, copper formate (20 g), zirconiagrinding balls (60 g), and anhydrous ethanol (20 mL) were added to

2 zirconia jars, and then placed in a planetary ball mill (MIQI, QM3SP2, Changsha, China) and milled for12 h at 300 rpm. After milling, the milled mixture was dried in a drying chamber at 70 ℃ for 6 h and then sieved by a stainless mesh.

BM-2: Pre-set preparation of Cu_4O_3/CSBC composite with a Cu_4O_3 mass ratio of 15 wt.%. The ball-milled copper formate (152.3 mg) and CSBC powders (425 mg) were added equally to 2 zirconia jars. Each jar was supplemented with grinding balls (12 g) and anhydrous ethanol (2.0 mL). Subsequently, the jars were transferred to a planetary ball mill, and subjected to ball milling for 1.5 h at 300 rpm. Following the ball milling process, the jars were placed in a drying chamber at 60 ℃ for 2 h to remove ethanol. Finally, the resulting copper formate/CSBC precursor powder was sieved by a stainless mesh screen.

Solid-state sintering process

Copper formate/CSBC precursor (20 mg) was put in a quartz crucible and transferred to the isothermal region of a box-type resistance furnace, the furnace was heated to 230 ℃ with a heating rate of 10 ℃ min^{-1} and maintained for 12 min. The Cu_4O_3/CSBC composite was finally obtained after air cooling to room temperature.

3.4.2. Quenching reactions

The box-type resistance furnace was heated to 230 ℃ and then waited for 10 min until the furnace temperature stabilized. The six quartz crucibles containing pre-prepared copper formate/CSBC precursor were put into the isothermal region rapidly and timing started immediately after the temperature stabilized at 230 ℃. When sintered at 230 ℃ for 2 min, one sample was immediately taken out by a crucible tongs, covered with aluminum foil, and placed in a dewar filled with liquid nitrogen for cooling (40 s). Similarly, the remaining 5 samples were taken out after sintering at 230 ℃ for 4 min, 6 min, 8 min, 10 min, and 12 min, respectively, and were quenched by rapid cooling with liquid nitrogen.

3.4.3. Determination of antibacterial properties

To assess the antibacterial properties of the Cu_4O_3/CSBC composite, Gram-negative Escherichia coli *E. coli*, Gram-positive Staphylococcus aureus *S. aureus*, and Methicillin-resistant Staphylococcus aureus *MRSA* were employed as model bacteria. The minimum inhibitory concentration (MIC) was tested using the oscillation method in accordance with the national standard of China "GB/T 21510 – 2008". Nutrient agar medium, nutrient broth, phosphate buffer solution (PBS, 0.03 mol L^{-1}), Petri dishes, conical flasks, test tubes, pipette tips, and filter paper were sterilized in an autoclave for 20 min at 121 ℃ and 103 kPa. Subsequently, nutrient agar medium (15 mL) was evenly distributed into a 90 mm diameter Petri dish and allowed to solidify at room temperature. *E. coli*, *S. aureus*, and *MRSA* were each inoculated into nutrient broth (100 mL) and incubated at 37 ℃ and 130 rpm for 18 h with shaking to achieve an initial inoculum suspension with a viable cell count of 10^8 CFU mL^{-1}. Following incubation, the bacterial solution was diluted to 10^3 CFU mL^{-1} using nutrient broth and PBS buffer solution.

The bacterial solution, PBS buffer solution, and various concentrations of the Cu_4O_3/CSBC composite solution were mixed in a volume ratio of 1:4:5. Following a 4-h incubation period at 37 ℃ and 150 rpm with shaking, the treated mixture (5 μL) was dropped onto a nutrient agar medium plate. Subsequently, the growth of bacteria was assessed following a 24-h incubation period at 37 ℃. The lowest concentration at which bacteria cease growing represents the MIC of the test sample. CSBC was employed as a control for the antibacterial test, with the tested concentration matching that of CSBC content (85 wt.%) in the Cu_4O_3/CSBC composite.

The three bacteria, *E. coli*, *S. aureus*, and *MRSA*, were sampled before and after the antibacterial test treatment, fixed with glutaraldehyde, and dehydrated in a gradient with anhydrous ethanol. The morphology of the bacteria before and after treatment with the Cu_4O_3/CSBC composite was observed by SEM.

3.4.4. Determination of release of copper ions

The release of Cu(I) ions was detected using bathocuproinedisulfonic acid disodium salt (BCS). The Cu_4O_3/CSBC composite (5 mg) was put into a double-necked round-bottomed flask containing BCS solution (20 mL) with a concentration of 0.5 mM. Inert gas displacement was performed sequentially by vacuum pump evacuation and nitrogen filling and circulated three times to exclude oxygen from the solution system. The suspension was then sonicated for 2 min and then stirred at 500 rpm and timed, the upper suspension (200 μL) was aspirated at 30 min, 1 h, 2 h, 6 h, 12 h, and 24 h, respectively. The recovered suspension was centrifuged and filtered through a 0.11 μm filter membrane to remove insoluble substances. UV-Vis spectroscopy was employed to measure the absorbance of the samples in the wavelength range of λ = 190–700 nm.

3.4.5. ROS test

The reactive oxygen species (ROS) generation capability of Cu_4O_3/CSBC composite was assessed using nitroblue tetrazolium (NBT) to detect superoxide anion ($\bullet O_2^-$). The Cu_4O_3/CSBC composite (5 mg) was placed into a beaker containing NBT solution (20 mL) with a concentration of 25 μM. The suspension was then ultrasonicated for 2 min followed by stirring at 500 rpm, with timing initiated upon stirring commencement. At intervals of 10 min, 20 min, 30 min, and 60 min, the upper suspension (200 μL) was aspirated, underwent centrifugation and filtration through a 0.11 μm filter membrane to eliminate insoluble substances. UV-Vis spectroscopy was utilized to measure the absorbance of the samples in the wavelength range of λ = 190–500 nm to assess changes in NBT concentration.

3.4.6. Computational methods

All density functional theory (DFT) calculations were performed by using the Vienna *ab initio* simulations package (VASP).[42] The interaction between valence electrons and ion cores is described by the projector augmented wave (PAW) method,[43], and plane waves with a kinetic energy cutoff of 520 eV were used for expanding electron wave functions. The exchange-correlation interaction is treated by the

Perdew-Burke-Ernzerhof (PBE) functional within the generalized gradient approximation (GGA).[44] The integration over the first Brillouin zone is performed on a uniformed **k**-point mesh with a grid density of ~ $2\pi \times 0.02$ $Å^{-1}$ along each periodic direction, that is 9×9×9 for bulk Cu_4O_3 and 4×8×1 for the slab models. The Hubbard-U correction with parameters $U = 7.5$ eV and $J = 0.98$ eV is adopted for the on-site repulsion of Cu-3d orbitals, which is widely used in Cu-O systems.[45]

4. Conclusion

In this study, the Cu_4O_3/biochar composite with superior antimicrobial properties was developed through the solid-state synthesis strategy of ball milling and sintering processes. This *in-situ* preparation method demonstrates the characteristics of simplicity, efficiency, eco-friendliness, and universality of the biochar source, achieving the high-purity and stable support of Cu_4O_3. The preparation mechanism of Cu_4O_3/CSBC composite was investigated, in which copper formate was used as the copper source, while biochar serves as the reducing agent, support carrier, and dispersant within the preparation and reaction system, playing a crucial role in regulating the stoichiometric ratio of Cu_2O and CuO. This preparation method achieved the first solid-state symproportionation reaction of copper oxides beyond liquid-phase methods.

The antibacterial test shows that the Cu_4O_3/CSBC composite exhibited highly efficient bactericidal effects against *E. coli*, *S. aureus*, and *MRSA*, particularly demonstrating significantly low MIC value against *S. aureus* and superbug *MRSA*. Furthermore, we analyzed the antibacterial mechanism of the Cu_4O_3/CSBC composite through experiment and DFT computational approaches, revealing the dual effects from both the slow successive release of Cu(I)/Cu(II) ions and the generation of ROS. The Cu_4O_3/CSBC composite is expected to be applied to public healthcare to enhance protection against pathogenic microbial infections, including superbugs. This solid-state synthesis approach prepares high-purity Cu_4O_3/CSBC composite via symproportionation reactions by combining ball milling and sintering processes and is anticipated to achieve large-scale preparation and broaden the application scope of Cu_4O_3.

Declarations

Conflict of Interest

The authors declare no conflict of interest.

Acknowledgements

We thank the financial supports of the National Natural Science Foundation of China (Nos. 52373227, 52201016, and 91641128) and the National Key R&D Program of China (Nos. 2017YFB0701502 and

2017YFB0702901). This work was also supported by the Shanghai Technical Service Center for Advanced Ceramics Structure Design and Precision Manufacturing (No. 20DZ2294000), and the Shanghai Technical Service Center of Science and Engineering Computing, Shanghai University. The authors acknowledge the Beijing Super Cloud Computing Center, Hefei Advanced Computing Center, and Shanghai University for providing HPC resources.

Data Availability Statement

The data that support the findings of this study are available from the corresponding author upon reasonable request.

References

1. a) R. E. Baker, A. S. Mahmud, I. F. Miller, M. Rajeev, F. Rasambainarivo, B. L. Rice, S. Takahashi, A. J. Tatem, C. E. Wagner, L.-F. Wang, *Nature Reviews Microbiology* **2022**, 20, 193; b) A. S. Fauci, D. M. Morens, *New England journal of medicine* **2012**, 366, 454; c) J. O. Lloyd-Smith, D. George, K. M. Pepin, V. E. Pitzer, J. R. Pulliam, A. P. Dobson, P. J. Hudson, B. T. Grenfell, *science* **2009**, 326, 1362.
2. a) S. Duan, R. Wu, Y.-H. Xiong, H.-M. Ren, C. Lei, Y.-Q. Zhao, X.-Y. Zhang, F.-J. Xu, *Progress in Materials Science* **2022**, 125, 100887; b) C. J. Murray, K. S. Ikuta, F. Sharara, L. Swetschinski, G. R. Aguilar, A. Gray, C. Han, C. Bisignano, P. Rao, E. Wool, *The lancet* **2022**, 399, 629.
3. Antimicrobial resistance.https://www.who.int/news-room/fact-sheets/detail/antimicrobial-resistance.2023.
4. a) Q. Zhang, K. Zhang, D. Xu, G. Yang, H. Huang, F. Nie, C. Liu, S. Yang, *Progress in Materials Science* **2014**, 60, 208; b) S. Behzadinasab, A. Chin, M. Hosseini, L. Poon, W. A. Ducker, *ACS applied materials & interfaces* **2020**, 12, 34723; c) J. Zhou, H. Xiang, F. Zabihi, S. Yu, B. Sun, M. Zhu, *Nano Research* **2019**, 12, 1453; d) M. L. Ermini, V. Voliani, *ACS nano* **2021**, 15, 6008.
5. P. Morgan, D. Partin, B. Chamberland, M. O'Keeffe, *Journal of solid state chemistry* **1996**, 121, 33.
6. L. Debbichi, M. Marco de Lucas, J. Pierson, P. Kruger, *The Journal of Physical Chemistry C* **2012**, 116, 10232.
7. Z. Jiang, S. Tian, S. Lai, R. D. McAuliffe, S. P. Rogers, M. Shim, D. P. Shoemaker, *Chemistry of Materials* **2016**, 28, 3080.
8. a) J. Medina-Valtierra, C. Frausto-Reyes, G. Camarillo-Martínez, J. A. Ramírez-Ortiz, *Applied Catalysis A: General* **2009**, 356, 36; b) D. S. Murali, A. Subrahmanyam, *Journal of Physics D: Applied Physics* **2016**, 49, 375102.
9. a) W. Wang, L. Zhu, P. Lv, G. Liu, Y. Yu, J. Li, *ACS applied materials & interfaces* **2018**, 10, 37287; b) L. Zhao, H. Chen, Y. Wang, H. Che, P. Gunawan, Z. Zhong, H. Li, F. Su, *Chemistry of Materials* **2012**, 24, 1136.

10. a) K. Weber, P. Quicker, *Fuel* **2018**, 217, 240; b) J. Wang, S. Wang, *Journal of Cleaner Production* **2019**, 227, 1002.
11. a) S. P. Sohi, E. Krull, E. Lopez-Capel, R. Bol, *Advances in agronomy* **2010**, 105, 47; b) J. Lehmann, A. Cowie, C. A. Masiello, C. Kammann, D. Woolf, J. E. Amonette, M. L. Cayuela, M. Camps-Arbestain, T. Whitman, *Nature Geoscience* **2021**, 14, 883.
12. a) R. Das, S. N. Panda, *Journal of Analytical and Applied Pyrolysis* **2022**, 167, 105691; b) R. P. Lopes, D. Astruc, *Coordination Chemistry Reviews* **2021**, 426, 213585.
13. a) Y. Yuan, N. Bolan, A. Prévoteau, M. Vithanage, J. K. Biswas, Y. S. Ok, H. Wang, *Bioresource technology* **2017**, 246, 271; b) J. Yuan, Y. Wen, D. D. Dionysiou, V. K. Sharma, X. Ma, *Chemical Engineering Journal* **2022**, 429, 132313.
14. a) X. Zhou, Y. Zhu, Q. Niu, G. Zeng, C. Lai, S. Liu, D. Huang, L. Qin, X. Liu, B. Li, *Chemical Engineering Journal* **2021**, 416, 129027; b) L. Liang, F. Xi, W. Tan, X. Meng, B. Hu, X. Wang, *Biochar* **2021**, 3, 255; c) W. Gwenzi, N. Chaukura, C. Noubactep, F. N. Mukome, *Journal of environmental management* **2017**, 197, 732.
15. H. K. S. Panahi, M. Dehhaghi, Y. S. Ok, A.-S. Nizami, B. Khoshnevisan, S. I. Mussatto, M. Aghbashlo, M. Tabatabaei, S. S. Lam, *Journal of cleaner production* **2020**, 270, 122462.
16. K. Sun, H. Hu, Z. He, Z. Xiao, X. Jin, C. Zheng, Y. Liu, *Carbohydrate Polymers* **2024**, 332, 121851.
17. a) H. Lyu, B. Gao, F. He, A. R. Zimmerman, C. Ding, H. Huang, J. Tang, *Environmental Pollution* **2018**, 233, 54; b) M. Naghdi, M. Taheran, S. K. Brar, T. Rouissi, M. Verma, R. Y. Surampalli, J. R. Valero, *Journal of Cleaner Production* **2017**, 164, 1394.
18. S. C. Peterson, M. A. Jackson, S. Kim, D. E. Palmquist, *Powder Technology* **2012**, 228, 115.
19. W.-J. Liu, H. Jiang, H.-Q. Yu, *Chemical reviews* **2015**, 115, 12251.
20. P. He, Y. Liu, L. Shao, H. Zhang, F. Lü, *Chemosphere* **2018**, 212, 385.
21. W. Suliman, J. B. Harsh, N. I. Abu-Lail, A.-M. Fortuna, I. Dallmeyer, M. Garcia-Perez, *Biomass and Bioenergy* **2016**, 85, 1.
22. M. A. Mohamed, A. K. Galwey, S. A. Halawy, *Thermochimica Acta* **2004**, 411, 13.
23. a) A. Tomczyk, Z. Sokołowska, P. Boguta, *Reviews in Environmental Science and Bio/Technology* **2020**, 19, 191; b) L. Leng, Q. Xiong, L. Yang, H. Li, Y. Zhou, W. Zhang, S. Jiang, H. Li, H. Huang, *Science of the total Environment* **2021**, 763, 144204; c) S. Li, S. Harris, A. Anandhi, G. Chen, *Journal of Cleaner Production* **2019**, 215, 890.
24. a) M. C. Enright, D. A. Robinson, G. Randle, E. J. Feil, H. Grundmann, B. G. Spratt, *Proceedings of the National Academy of Sciences* **2002**, 99, 7687; b) S. Stefani, D. R. Chung, J. A. Lindsay, A. W. Friedrich, A. M. Kearns, H. Westh, F. M. MacKenzie, *International journal of antimicrobial agents* **2012**, 39, 273.
25. B. Li, Y. Li, Y. Zhao, L. Sun, *Journal of Physics and Chemistry of Solids* **2013**, 74, 1842.
26. R. Salah, M. Karmy, A. Abdelraouf, S. Kotb, *Journal of Veterinary Medical Research* **2020**, 27, 143.
27. C.-S. Chien, C.-J. Lin, C.-J. Ko, S.-P. Tseng, C.-J. Shih, *Journal of Alloys and Compounds* **2018**, 747, 1.

28. A. C. M. de Moraes, B. A. Lima, A. F. de Faria, M. Brocchi, O. L. Alves, *International journal of nanomedicine* **2015**, 6847.
29. T. Kruk, K. Szczepanowicz, J. Stefańska, R. P. Socha, P. Warszyński, *Colloids and Surfaces B: Biointerfaces* **2015**, 128, 17.
30. H. Q. Raheem, L. H. Al-Ghazali, F. A. Al-Marzook, *International Journal of Pharmaceutical Quality Assurance* **2019**, 10.
31. A. Hassan, F. A. Al-Salmi, M. A. Saleh, J.-M. Sabatier, F. A. Alatawi, M. A. Alenezi, F. M. Albalwe, H. Meteq R. Albalawi, D. B. E. Darwish, E. M. Sharaf, *ACS Omega* **2023**, 8, 9969.
32. A. E. Rashid, M. E. Ahmed, M. K. Hamid, *Int J Drug Deliv Technol* **2022**, 12, 985.
33. N. H. Harun, R. B. S. M. N. Mydin, S. Sreekantan, K. A. Saharudin, N. Basiron, F. Aris, W. N. Wan Mohd Zain, A. Seeni, *ACS Omega* **2020**, 5, 12027.
34. a) C. E. Santo, N. Taudte, D. H. Nies, G. Grass, *Applied and environmental microbiology* **2008**, 74, 977; b) J. Zhou, H. Xiang, F. Zabihi, S. Yu, B. Sun, M. Zhu, *Nano Research* **2019**, 12, 1453.
35. a) X. Chen, G. Chen, L. Chen, Y. Chen, J. Lehmann, M. B. McBride, A. G. Hay, *Bioresource technology* **2011**, 102, 8877; b) X.-j. Tong, J.-y. Li, J.-h. Yuan, R.-k. Xu, *Chemical Engineering Journal* **2011**, 172, 828.
36. a) T. M. Gross, J. Lahiri, A. Golas, J. Luo, F. Verrier, J. L. Kurzejewski, D. E. Baker, J. Wang, P. F. Novak, M. J. Snyder, *Nature Communications* **2019**, 10, 1979; b) K. Sunada, M. Minoshima, K. Hashimoto, *Journal of Hazardous Materials* **2012**, 235-236, 265; c) E. Santo Christophe, N. Taudte, H. Nies Dietrich, G. Grass, *Applied and Environmental Microbiology* **2008**, 74, 977.
37. C. Campos, R. Guzmán, E. López-Fernández, Á. Casado, *Analytical Biochemistry* **2009**, 392, 37.
38. a) N. E. Grossoehme, A. M. Spuches, D. E. Wilcox, *JBIC Journal of Biological Inorganic Chemistry* **2010**, 15, 1183; b) D. K. Johnson, M. J. Stevenson, Z. A. Almadidy, S. E. Jenkins, D. E. Wilcox, N. E. Grossoehme, *Dalton transactions* **2015**, 44, 16494.
39. L. Debbichi, M. C. Marco de Lucas, P. Krüger, *Materials Chemistry and Physics* **2014**, 148, 293.
40. X. Zhu, D. Wu, W. Wang, F. Tan, P. K. Wong, X. Wang, X. Qiu, X. Qiao, *Journal of Alloys and Compounds* **2016**, 684, 282.
41. F. Li, N. Li, C. Xue, H. Wang, Q. Chang, H. Liu, J. Yang, S. Hu, *Chemical Engineering Journal* **2020**, 382, 122484.
42. a) G. Kresse, J. Furthmüller, *Physical review B* **1996**, 54, 11169; b) G. Kresse, J. Furthmüller, *Computational materials science* **1996**, 6, 15.
43. P. E. Blöchl, *Physical review B* **1994**, 50, 17953.
44. J. P. Perdew, K. Burke, M. Ernzerhof, *Physical review letters* **1996**, 77, 3865.
45. D. Wu, Q. Zhang, M. Tao, *Physical Review B* **2006**, 73, 235206.

Figures

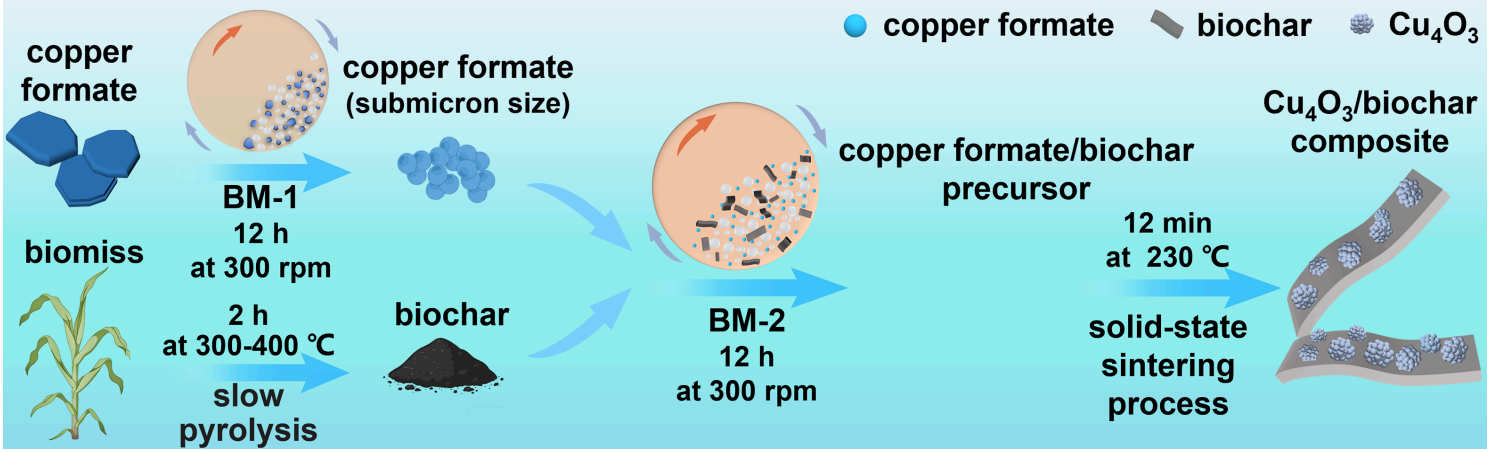

Figure 1

Schematic diagram of the solid-state preparation process for the Cu_4O_3/biochar composite.

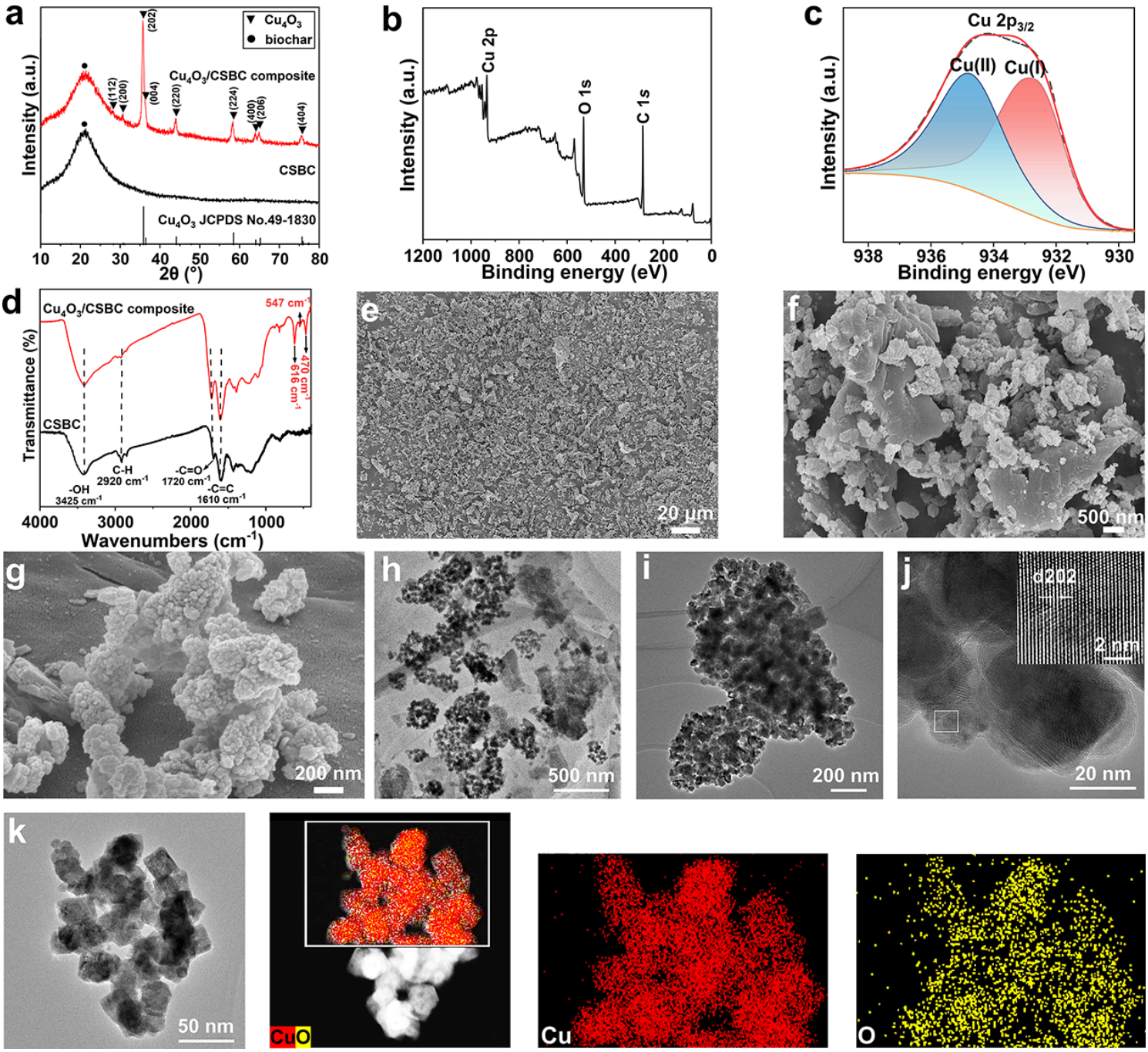

Figure 2

Characterizations of the Cu_4O_3/CSBC composite. a) XRD patterns of CSBC and the Cu_4O_3/CSBC composite. b) XPS survey spectrum and c) Cu 2p spectrum of the Cu_4O_3/CSBC composite. d) FTIR spectra of CSBC and the Cu_4O_3/CSBC composite. e-g) Low and high magnification SEM micrographs of the Cu_4O_3/CSBC composite. h-j) TEM images of the Cu_4O_3/CSBC composite. k) EDX elemental mapping of the Cu_4O_3 for the elements Cu, and O, respectively.

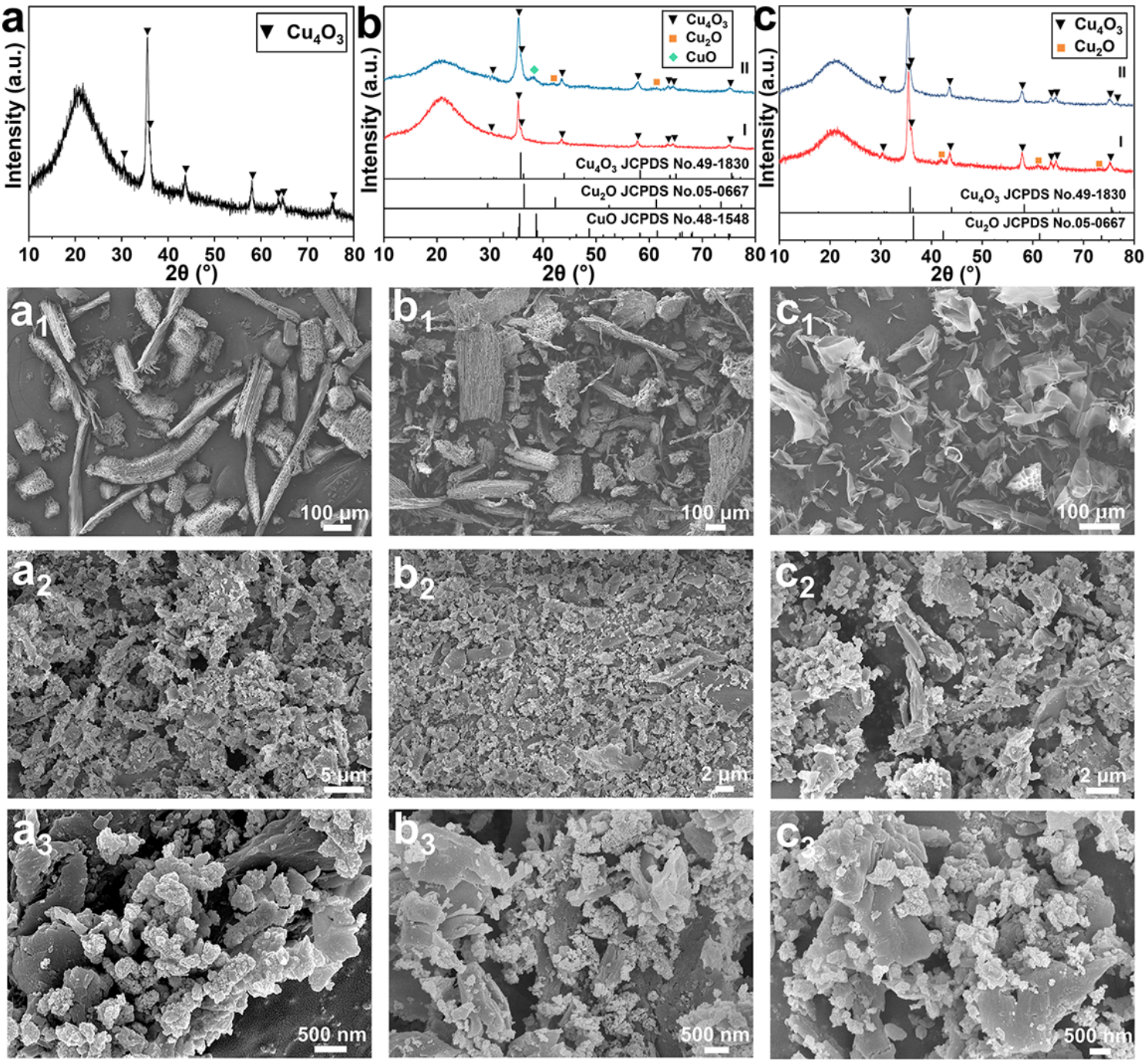

Figure 3

The characterizations of the sintered product for the various types of biochar and copper formate after the BM-2 and solid-state sintering processes. a) XRD spectrum of the sintered product for copper formate/PLBC precursor. b) XRD spectra of the sintered product of copper formate/CWBC precursor. b_I: at a support amount of 10 wt.% of Cu_4O_3; b_{II}: at a support amount of 15 wt.% of Cu_4O_3. c) XRD spectra of the sintered product of copper formate/BBC precursor. c_I: BBC pyrolysis temperature at 300 °C; c_{II}: BBC pyrolysis temperature at 400 °C. $a_{1\text{-}3}$) SEM micrographs of (a_1) PLBC and ($a_{2\text{-}3}$) the Cu_4O_3/PLBC composite. $b_{1\text{-}3}$) SEM micrographs of (b_1) CWBC and ($b_{2\text{-}3}$) the Cu_4O_3/CWBC composite. $c_{1\text{-}3}$) SEM micrographs of (c_1) BBC and ($c_{2\text{-}3}$) the Cu_4O_3/BBC composite.

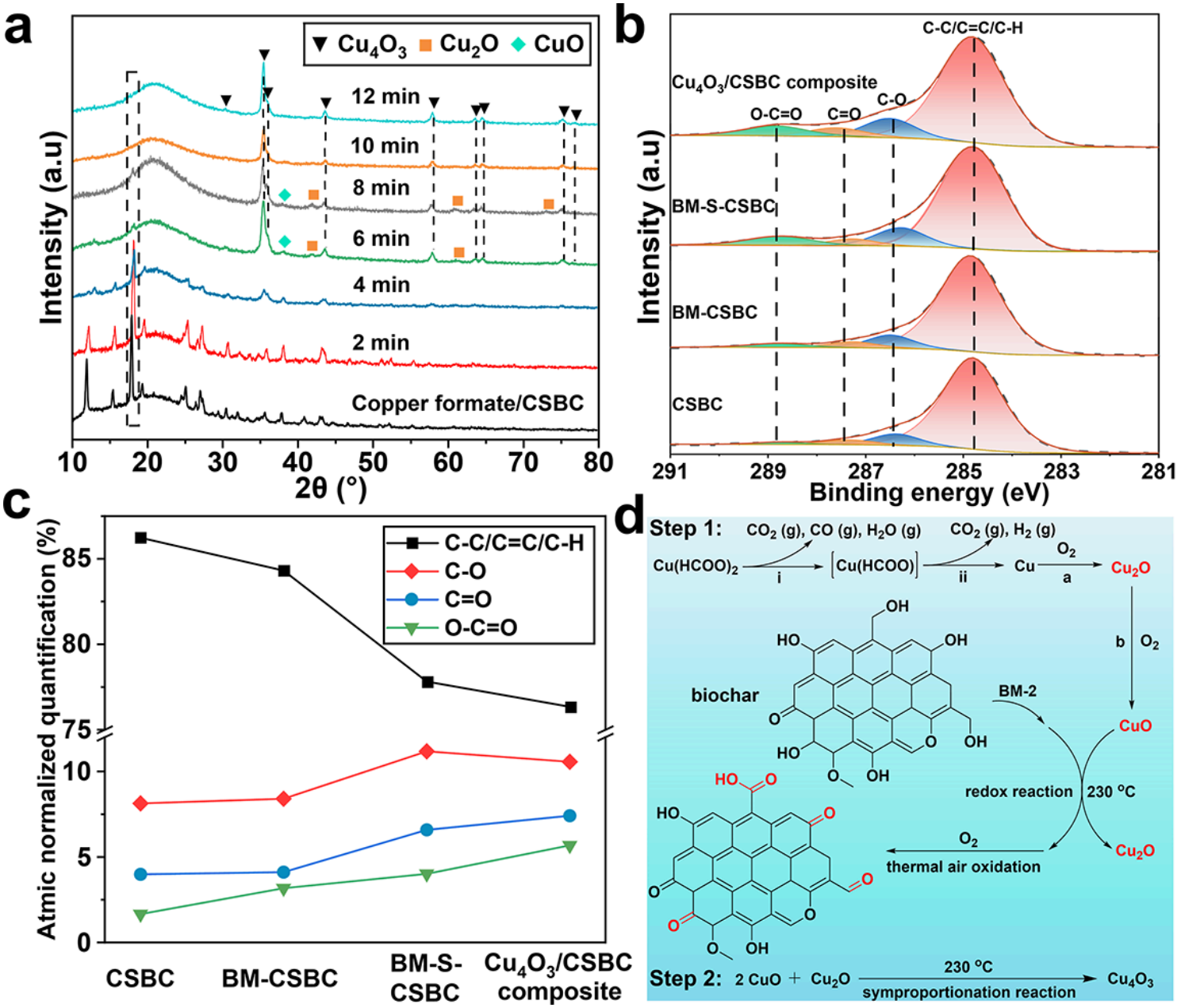

Figure 4

The formation mechanism analysis of the Cu_4O_3/CSBC composite. a) XRD spectra of the sintered products for copper formate/CSBC precursor at 230 ℃ at various sintering times (0 min-12 min) after rapid cooling process with liquid nitrogen. b) The C 1s spectra and their fitting results of CSBC, BM-CSBC, BM-S-CSBC and Cu_4O_3/CSBC composite. c) The normalized quantitative analysis of C 1s spectra fitting results. d) Schematic diagram of the reaction mechanism for the preparation of the Cu_4O_3/CSBC composite.

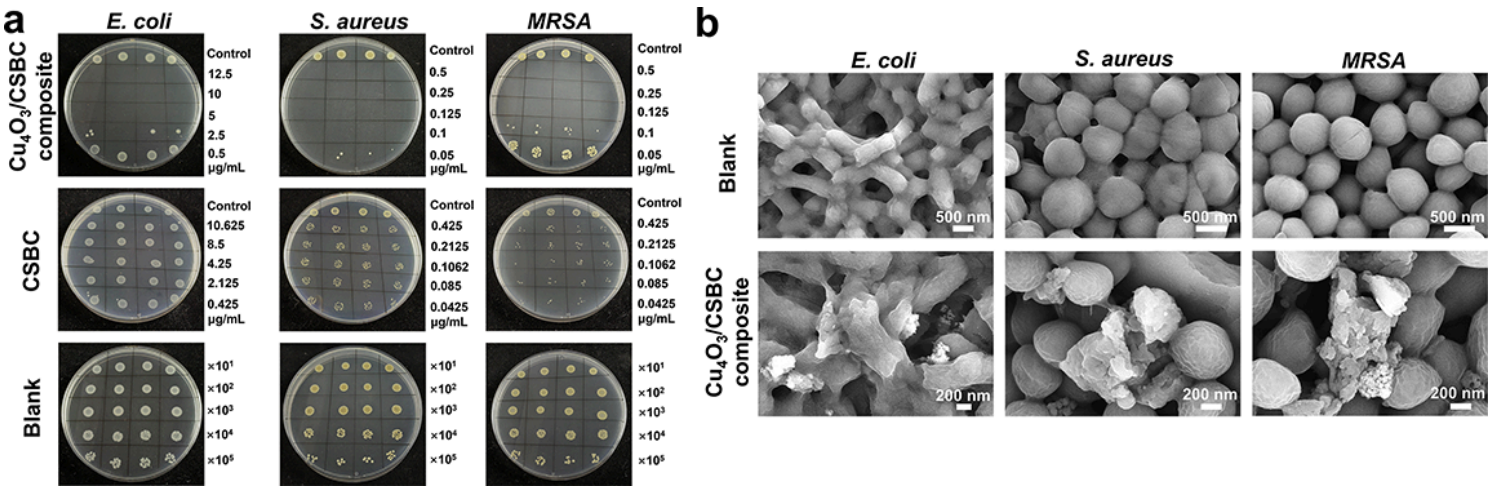

Figure 5

The antibacterial property analysis of Cu_4O_3/CSBC composite. a) The MIC test images of the Cu_4O_3/CSBC composite against *E. coli*, *S. aureus*, and *MRSA*, respectively. CSBC and blank groups as controls. b) Surface morphology of *E. coli*, *S. aureus*, and *MRSA* before and after treatment by the Cu_4O_3/CSBC composite.

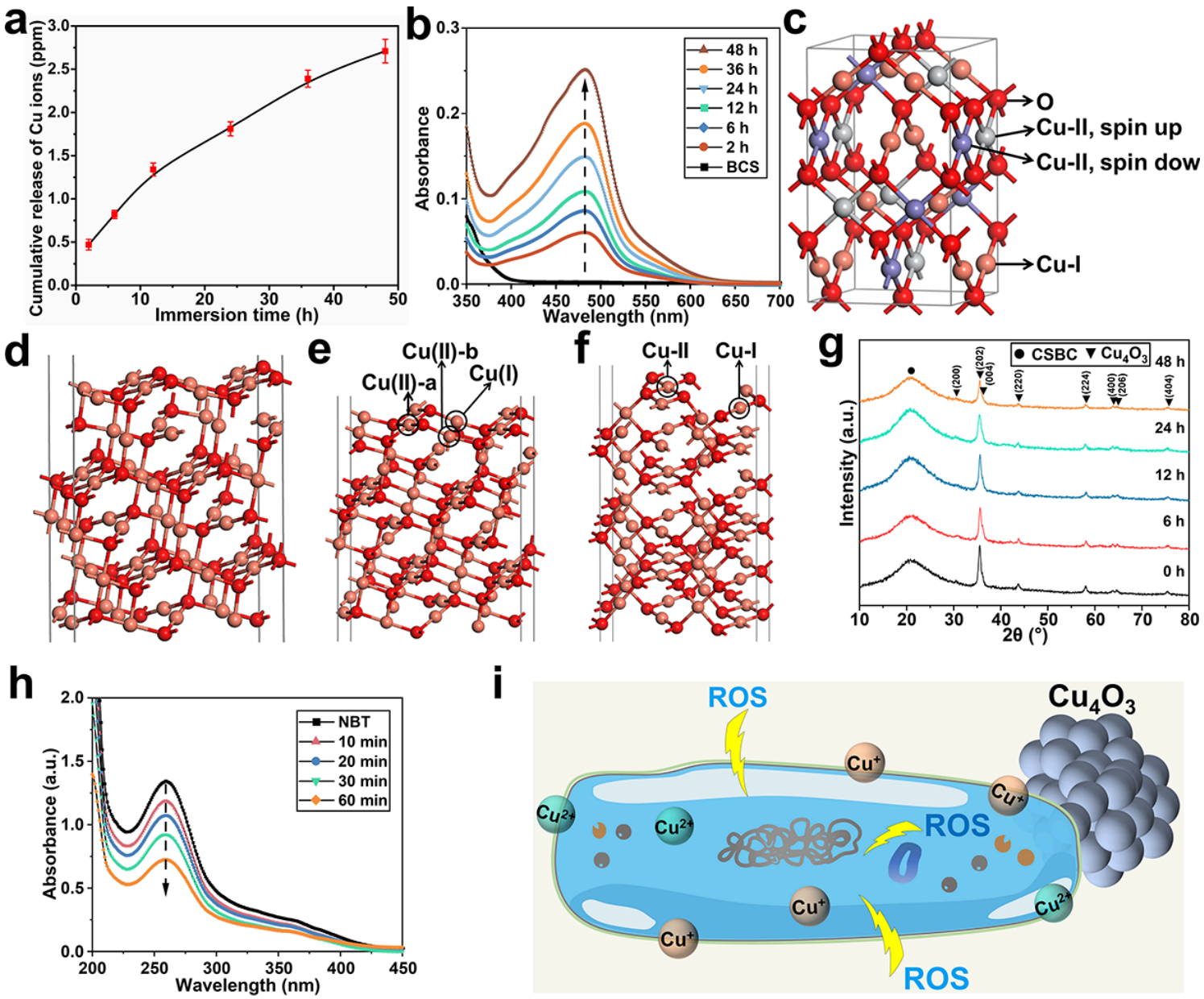

Figure 6

Antibacterial mechanism analysis of the Cu_4O_3/CSBC composite. a) The cumulative release of Cu ions during the 48-h immersion for the Cu_4O_3/CSBC composite. b) The absorbance of BCS treated with the Cu_4O_3/CSBC composite within a 48-h test period. c) Ball-and-stick model of Cu_4O_3 with body-centered tetragonal lattice, $I4_1/amd$ (no. 141) space groups. d) Cu_4O_3 (101) surface model after structural optimization. e) Three types of Cu ions on the Cu_4O_3 (101) surface model. f) Cu_4O_3 (100) surface model with the two types of Cu ions. g) The XRD spectra of the Cu_4O_3/CSBC composite during the 48-h immersion experiment. h) The absorbance of NBT treated with the Cu_4O_3/CSBC composite within a 48-h test period. i) The antimicrobial mechanism schematic of the Cu_4O_3/CSBC composite.

Supplementary Files

This is a list of supplementary files associated with this preprint. Click to download.

- Cu4O3SKCEJSI.docx